Hierarchically Porous, Ultra-strong Reduced Graphene Oxide-Cellulose Nanocrystal Sponges for Exceptional Adsorption of Water Contaminants

Nariman Yousefi[1†], Kerwin K.W. Wong[1,2†], Zeinab Hosseinidoust[1,3], Henning Osholm Sørensen[4], Stefan Bruns[4], Yi Zheng[5], Nathalie Tufenkji[1]*

[1]Department of Chemical Engineering, McGill University, Montreal, QC, Canada

[2]Department of Chemical Engineering, University of Leuven, Leuven, Belgium

[3]Current affiliation: Department of Chemical Engineering, McMaster University, Hamilton, ON, Canada

[4]Nano-Science Center, Department of Chemistry, University of Copenhagen, Universitetsparken 5, 2100 Copenhagen Ø, Denmark

[5]Department of Physics, Technical University of Denmark, 2800 Kongens Lyngby, Denmark

* Corresponding Author. Phone: (514) 398-2999; Fax: (514) 398-6678; e-mail: nathalie.tufenkji@mcgill.ca

[†] Equal contribution

Abstract

Self-assembly of graphene oxide (GO) nanosheets into porous 3D sponges is a promising approach to exploit their capacity to adsorb contaminants while facilitating the recovery of the nanosheets from treated water. Yet, forming mechanically robust sponges with suitable adsorption properties presents a significant challenge. Ultra-strong and highly porous 3D sponges are formed using GO, vitamin C (VC), and cellulose nanocrystals (CNCs) – natural nanorods isolated from wood pulp. CNCs provide a robust scaffold for the partially reduced GO (rGO) nanosheets resulting in an exceptionally stiff nanohybrid. The concentration of VC as a reducing agent plays a critical role in tailoring the pore architecture of the sponges. By using excess amounts of VC, a unique hierarchical pore structure is achieved, where VC grains act as soft templates for forming millimeter-sized pores, the walls of which are also porous and comprised of micron-sized pores. The unique hierarchical pore structure ensures the interconnectivity of pores even at the core of large sponges as evidenced by micro and nano X-Ray computed tomography. The unique pore architecture translates into an exceptional specific surface area for adsorption of a wide range of contaminants, such as dyes, heavy metals, pharmaceuticals and cyanotoxins from water.

Keywords: graphene, 3D nanostructure, water treatment, cellulose nanocrystal, vitamin C

1. Introduction

Graphene-based hydrogels (sponges) are recognized as one of the most promising nanostructures for a wide range of applications where high performance porous materials are needed; namely, as supercapacitors[1, 2], lithium ion batteries[3, 4], structural nanocomposites[5], and as filters for air, water and wastewater treatment[6-8]. High specific surface area and availability of interconnected pores are critical to the performance of graphene-based sponges for many of these applications. The rational assembly of graphene oxide (GO) nanosheets – the strongest nanomaterial that possesses the highest theoretical specific surface area[9, 10]– into a 3D porous architecture not only exploits the plethora of active sites available on nanoscale GO, but also immobilizes these nanosheets into a bulk structure. This is particularly important for applications such as air or water treatment, where recovery of potentially toxic suspended nanoparticles from treated air or water poses a significant challenge.

Although GO is one of the strongest materials ever known, the mechanical properties of its sponges are critically influenced by the bonding strength between GO nanosheets. Additionally, GO nanosheets are thermodynamically metastable and tend to revert back to a layered graphite-like structure once they are destabilized in an aqueous medium[11]. Introduction of 1D nanomaterials such as carbon nanotubes (CNTs) provides a geometrical barrier where the face-to-face assembly of GO nanosheets is hindered[12, 13]. For GO sponges, this geometrical barrier translates into improved porosity and stronger sponges.

Cellulose nanocrystals (CNCs) are 1D crystalline nanorods that are isolated from semi-crystalline cellulose, the most abundant natural polymer, through selective dissolution of the amorphous segments of cellulose fibers. Unlike CNTs[14, 15], there have not been any major reports on the health risks and cytotoxicity of CNCs[16]. Moreover, the mechanical properties of CNCs are comparable with that of Kevlar fibers and on par with CNTs[17, 18]. Similar to GO, the surface of CNCs is decorated with a myriad of carboxyl and hydroxyl groups which renders them hydrophilic and highly dispersible in water. This unique property of CNCs is in contrast with the hydrophobic nature of pristine CNTs, which hinders their processing in aqueous media. The high aspect ratio, remarkable mechanical properties, low cost of processing and natural feedstock of CNCs make them an attractive option in designing mechanically strong GO based sponges[17, 18]. Additionally, CNCs have already been extensively used for water treatment applications, showing remarkable absorption capacity towards heavy metal ions, dyes and other organic pollutants[17].

The loss of effective surface area of GO after self-assembly into sponge form is a major challenge in designing high performance adsorptive materials. The restacking of GO sheets, and most importantly, the lack of interconnectivity between pores (closed pores), especially in the middle of large sponges contribute to the decrease in specific surface area of sponges in comparison with particulate GO. Rational self-assembly of GO nanosheets into hierarchically porous sponges comprised of interconnected large pores located in a matrix of porous material with smaller pores is a solution to avoid significant decrease of effective surface area upon self-assembly of GO nanosheets[19-21].

The main objective of this work is to design sponges with superior mechanical properties and high adsorption capacity towards a wide range of water contaminants. Partially reduced GO (rGO)-CNC hybrid sponges were processed using the natural reducing agent vitamin C (VC). Granules of the green reactant VC, added in excess to mixtures of GO and CNCs, acted as soft templates, leading to formation of sponges with hierarchical pore structures. This is the first report on the design of an rGO based hierarchical 3D porous structure using VC as a soft template. The pores at millimeter, micrometer and sub-micrometer length-scales provided a highly interconnected platform for efficient molecular level adsorption of dissolved contaminants. Use of 1D CNCs in conjunction with 2D rGO nanosheets had a significant synergistic effect on the mechanical properties of the nanocomposite sponges. The sponges not only showed superior adsorption capacity towards classical water contaminants, but also efficiently removed emerging contaminants such as pharmaceuticals and a cyanotoxin. The hybrid ultra-strong sponge, formed using a mild and green processing method, holds great promise for purification of air and water.

2. Experimental Section

2.1. Processing of GO and CNC

GO was processed using a modified Hummers method[22]. Briefly, graphite (natural graphite, Ausbury Mills) was thermally expanded at 1050 °C for 15 s. 0.5 g of the resulting expanded graphite was mixed with 100 mL of sulfuric acid (Fisher) in a round bottom flask. Subsequently, 5 g of $KMnO_4$ (Sigma-Aldrich) were slowly added to the flask and the mixture was stirred at 200 rpm for 24 hrs in a 45 °C water bath. The reaction flask was then transferred into an ice bath and 125 mL of a 4:1 mixture of deionized (DI) water:H_2O_2 (Fisher) was added in a drop-wise manner to the flask mixture. After stirring for 30 min, the light brown reaction mixture was washed through successive centrifugation using 10% HCl (Fisher) solution and DI water at a maximum relative centrifugal force (rcf) of 18,000*g*. Each wash consisted of decantation of the supernatant and re-suspension of the resulting pellet in HCl solution or DI water. A total of 3 HCl and 5 DI water wash cycles were performed. The final concentration of the GO dispersion was 4 mg mL^{-1}.

The processing method for isolation of CNCs is described elsewhere[16, 23]. In short, 10 g of Q-90 softwood pulp was soaked in 250 mL DI water overnight, manually disintegrated by a spatula and reclaimed using a nylon mesh. The softwood pulp was transferred into a beaker and was reacted with 0.093 M $NaIO_4$ (Sigma-Aldrich) and 1 M NaCl (Fisher) for 96 hrs. Next, 4% ethylene glycol (Sigma-Aldrich) was added to the mixture to stop the periodate reaction and the treated pulp was vigorously washed with DI water to remove unreacted species and ions. The treated pulp – rich in aldehydes at this stage – was re-suspended in DI water at a concentration of 20 g mL^{-1}. Next, 1 M NaCl, 0.26 M NaClO (Sigma-Aldrich) and 0.26 M H_2O_2 (Fisher) was added to the mixture and stirred for 24 hours to convert the aldehydes to carboxyl groups. The pH of the mixture was maintained at 5 using 1 M NaOH solution. Finally, CNCs were separated from the mixture by 10 min centrifugation at an rcf of 26,000*g*, the nanocrystals in the supernatant were then precipitated by adding ethanol and redispersed in DI water at a concentration of 20 mg mL^{-1} after centrifugation (20,000*g* rcf, 10 min).

2.2. Preparation of hybrid sponges

The preparation method for rGO-VC and rGO-CNC sponges is schematically shown in Figure 1a and b. To prepare the hybrid sponges, 40 mg of GO was mixed with appropriate amounts of CNCs in a glass vial to achieve GO:CNC mass ratios of 4:1, 2:1, 1:1 and 1:2. Next, 6 g of VC was added to each mixture to achieve a GO:VC mass ratio of 1:150 and vigorously mixed through at least 5 min vortexing and 5 min bath sonication. The glass vials were transferred to a water bath at 95 °C. After 2, 5 and 10 minutes of residing in the water bath, the vials were further vortexed to promote homogeneous dispersion of the sponge components. The color of the mixtures gradually changed from brown to black due to chemical reduction of GO to rGO by VC. The vials were then left undisturbed in the water bath for 50 min. The dispersions self-assembled into porous sponges at the end of the heat treatment (Figure 1b). The sponges were gently washed with copious amounts of DI water (at least 10 times) to ensure complete removal of unreacted species. The samples were designated as rGO:CNC *x:y*, where *x:y* denotes the ratio of initially mixed GO:CNC. For the samples without CNCs, 40 mg GO were mixed with the corresponding amount of VC to obtain rGO sponges with 1:1 up to 1:300 rGO:VC mixing ratios (Figure 1a). These samples were designated as rGO:VC *z*, where *z* denotes the 1:*z* ratio of initially mixed GO:VC.

2.3. Sponge characterization

The morphology and pore size of the sponges were investigated using a scanning electron microscope (SEM, Hitachi SU3500) using secondary electrons accelerated at 5 kV. The freeze fractured samples were freeze dried at -80 °C for 24 hrs prior to SEM imaging. For studying the formation of CNC scaffolds within rGO:CNC sponges, the samples were cut with a razor blade in wet state and subsequently freeze dried at -80 °C for 24 hrs. VC reduction resulted in partial restoration of the sp^2 carbons which imparted electrical conductivity to the samples; hence, they were not sputter coated with a conductive alloy. Transmission electron microscopy (TEM, Tecnai G^2 F20) was used to study the morphology of rGO:CNC sponges at the nanoscale. 5 mg of rGO:CNC 2:1 sponge was mechanically crushed and dispersed in ethanol. Approximately 100 µL of the ethanol dispersion was drop cast on a carbon coated grid, which was subsequently dried in air and examined by TEM. The surface chemistry of the sponges was studied using X-ray photoelectron spectroscopy (XPS, Thermo Scientific K-Alpha). Freeze dried samples were studied using a monochromatic Al K_α X-ray source under a 10^{-8} mbar vacuum. High resolution C_{1s} peaks were recorded and deconvoluted to their constituent peaks using XPSPEAK41 software. The storage modulus of the sponges in the wet state was measured using a rheometer (TA Instruments AR-2000) in a parallel plate setup. Thin slices of the sponges were cut with a sharp surgical blade and placed between the parallel plates. The sponges were coated with a thin layer of silicone oil to avoid the discharge and evaporation of water. The samples were investigated in a frequency sweep mode (0.1–100 Hz) at a constant strain of 0.002. A dynamic mechanical analyzer (DMA, TA Instruments Q800) was used to measure the compressive storage modulus and to investigate the cyclic load-unload response of the sponges using a parallel plate compression module. Raman spectra were collected using a Raman confocal microscope (Bruker Senterra) equipped with a He–Ne laser at a wavelength of 532 nm. Thermogravimetric analysis (TGA, Perkin Elmer TGA7) was used to investigate the decomposition behavior of hybrid sponge components. The sponges were exposed to a temperature range of 25–600 °C at a ramp rate of 10 °C min^{-1} under a protective nitrogen atmosphere.

2.4. X-ray tomography

The 3D pore structure of the sponges was characterized by X-ray tomography. rGO:VC 150 and rGO:CNC 2:1 sponges were imaged at the Imaging Industry Portal at the Technical University of Denmark using an X-ray microtomography (microCT, Zeiss Xradia VersaXRM-410) instrument. The X-ray source was operated with an accelerating voltage of 40 kV, and the Bremsstrahlung spectrum from the W anode was utilized without additional filters. While rotating the samples 360°, 4001 projections were recorded with an exposure time of 15 s for each projection. The projections were recorded using the large field-of-view detector in unbinned mode, *i.e.* 2048 by 2048 pixels with an effective pixel size of 10.79 µm. The data were reconstructed using the instrument's built-in implementation of filtered back projection. Subsequently, the obtained data sets (Figure S1a, b) were noise filtered using an iterative implementation of a 3D non-local means algorithm[24, 25] (Figure S1c, d). The segmentation was done by a custom made Python script doing simple thresholding followed by removal of small misclassified (isolated) regions. The code used

Fabio for reading and writing images[26] (Figure S1c, d). The largest region spanning the bulk material was selected for both data sets. For rGO:VC 150 sponge, the final 3D image was 1360×1360×549 voxels (14.9×14.9×5.9 mm) and for rGO:CNC 2:1 it was 1360×1360×500 voxels (14.9×14.9×5.4 mm).

The nanotomography measurements were performed using a full field hard X-ray microscope (nanoCT, SPring-8 beamline BL37XU, Japan) providing an effective pixel size of 48.4 nm[27]. Small portions of rGO:VC 150 and rGO:CNC 2:1 sponges were cut from the freeze dried samples with a scalpel and mounted in vacuum grease on a brass pin. All data sets were collected by rotating the samples 180° while recording 1,800 projections with an exposure time of 250 ms. The projection data were dark current and bright field corrected. The truncated sinograms (since the field of view was smaller than the sample dimensions) were completed[28] and stripes were removed for ring artifact reduction[29] before reconstructing the 3D volume using the GridRec algorithm implemented in TomoPy[30]. Image noise was reduced using the 3D iterative nonlocal means method[24, 25]. The resulting images were cropped to volumes of 1020×1020×1004 voxels (49.4×49.4×48.6 µm) and segmented by marker based watershed segmentation. Seed locations for the segmentation were chosen by manually selecting two uniform thresholds for all datasets that mark certain background and foreground phases.

A morphological description of the samples was achieved by calculating chord length distribution functions for 10^6 randomly orientated chords in the void space as well as in the material phase of the segmented 3D images[24, 31]. We provide the mean (average) and the mode of the resulting distribution functions as a measure of scale for the sponges. The mode of the distribution functions was determined from a continuous density function after applying a kernel density estimate by using the interquartile range as a bandwidth selector and an Epanechnikov window[32].

2.5. Contaminant adsorption

Methylene blue (MB, Sigma-Aldrich) and, Cu^{2+} ($CuSO_4$, Sigma-Aldrich) and Cd^{2+} ($Cd(NO_3)_2$, Sigma-Aldrich) were used as model organic dye contaminant and heavy metal ions, respectively. Sulfamethoxazole (SMX, Sigma-Aldrich) and tetracycline (TC, Sigma-Aldrich), two important antibiotics, diclofenac (DCF, Sigma-Aldrich), a non-steroidal anti-inflammatory drug, and 17-α-ethynylestradiol (EE2, Sigma-Aldrich), a synthetic hormone, were selected as representative emerging contaminants. Microcystin-LR (Cayman Chemical) is a cyanotoxin produced by various cyanobacteria and was used as a representative environmental toxin.

Batch adsorption experiments were performed using 30 mg rGO:CNC 2:1 sponges placed in a 600 mL beaker to investigate contaminant adsorption kinetics, and to record the adsorption isotherms. In a typical kinetics experiment, a 200 mL aqueous solution of the contaminant (at a known concentration) was transferred into the beaker. Sponges with known rGO and CNC content were then introduced to the beaker under continuous mixing by a platform shaker (New Brunswick Instruments). 250 µL aliquots of the aqueous solution were removed after 0, 5, 10, 15, 20, 30, 60, 120, 180 and 240 min for measuring the concentration of the remaining dissolved contaminant using the respective analytical methods reported below. Contaminant adsorption by a sponge at time t, q_t (mg of adsorbate/g of adsorbent) was calculated using:

$$q_t = \frac{(C_0 - C_t)V}{W} \tag{1}$$

where W (mg) is the mass of adsorbent (sponge), V (mL) is the total liquid volume of the contaminant solution in the system and C_0 and C_t (mg L^{-1}) are the liquid phase concentrations of contaminant at time 0 (start of the experiment) and the different sampling times t, respectively.

The data was fitted with pseudo-first order (Eq. 2) and pseudo-second order (Eq. 3) kinetic models that are commonly used to study the nature of contaminant adsorption on sorbents[33-35].

$$\ln\left(q_{\mathrm{eq,exp}} - q_t\right) = \ln q_{\mathrm{eq,cal}} - \mathrm{k}_1 t \tag{2}$$

$$\frac{t}{q_{\mathrm{t}}} = \frac{1}{\mathrm{k}_2 q_{\mathrm{eq,exp}}^2} + \frac{t}{q_{\mathrm{eq,cal}}} \tag{3}$$

To determine the adsorption isotherms, batch experiments were conducted using four different initial concentrations and aliquots were measured until the contaminant concentration reached equilibrium (q_{eq}). q_{eq} values were calculated using Eq. 1 and were fitted using the classical Langmuir (Eq. 4) or Freundlich (Eq. 5) models[36]:

$$\frac{1}{q_{\mathrm{eq}}} = \frac{1}{q_{\mathrm{max}}} + \left(\frac{1}{k_{\mathrm{L}} q_{\mathrm{max}}}\right)\frac{1}{C_{\mathrm{eq}}} \tag{4}$$

$$\ln q_{\mathrm{eq}} = \ln k_{\mathrm{F}} - \frac{1}{n}\ln C_{\mathrm{eq}} \tag{5}$$

The reusability of the sponges was evaluated by saturating a rGO:CNC 2:1 sample with MB, and then washing the sponge with 4M sulfuric acid until the effluent became visually clear. The sponge was then washed with copious amounts of DI water to remove acid, and then reused for additional cycles of MB adsorption or for conducting rheometry tests.

The concentrations of MB and TC were measured using UV-Vis spectrophotometry (Tecan Infinite 200 PRO microplate reader) as they have a distinct absorption peak at 664 and 357 nm, respectively. Clear 96-well plates (Corning) were used for measurements, whereby the wells were filled with 250 μL aliquot samples. Inductively coupled plasma-atomic emission spectroscopy (ICP-AES, Icap 6000, Thermo Fisher Scientific) was used to measure the concentration of Cu^{2+}

and Cd^{2+}. Standard concentration-emission curves were developed for each heavy metal. For SMX, DCF, EE2 and cyanotoxin, high pressure liquid chromatography (HPLC) analysis was conducted on an Agilent 1050 HPLC system equipped with an autosampler, a quaternary pump and a variable wavelength detector with a cell volume of 11 µL. The emerging contaminants (SMX, EE2 and DCF) and cyanotoxin were detected by measuring absorbance at 270 and 238 nm, respectively and standard concentration-absorbance curves were developed for each compound. All experiments were performed in triplicate and at room temperature (~22 °C).

3. Results and Discussion

3.1. Engineering the sponge pore architecture with excess amounts of VC

The adsorption capacity of GO and rGO sponges is strongly dependent on their pore structure; while highly porous structures are desirable, the interconnectivity of pores, especially those situated away from the sponge surface, plays a dominant role in providing full access to the exceptionally large surface area offered by GO (and rGO) nanosheets. However, a highly porous sponge is usually obtained at the cost of decreased mechanical properties. A major motivation of this work is to synthesize highly porous, yet ultra-strong rGO sponges by rationally designing their self-assembly process. Use of excessive amounts of VC as a natural reducing agent, as well as incorporation of 1D CNCs are two tools for tailoring the self-assembly process of nanosheets to obtain ultra-strong sponges, having a unique hierarchical and interconnected pore structure.

The preparation method for rGO-VC and rGO-CNC sponges is schematically shown in Figure 1a and b. The freeze-fractured microstructure of the sponges at various VC and CNC contents is also shown in Figure 1c-r. A GO:VC ratio of 1:3 to 1:4 has been estimated to be the stoichiometric condition for reducing GO[37, 38]; however, for forming sponges, an excess amount of VC is required. Interaction with VC results in partial reduction of oxygen containing functional groups of GO, which subsequently translates into restoration of more hydrophobic sp^2 domains comprised of aromatic groups on the nanosheets; the hydrophobic and π-π interactions between partially reduced GO nanosheets have been identified as the mechanism of sponge formation with VC[39, 40]. GO concentration, gelling temperature and medium pH are also key factors governing sponge formation[39, 40]. Although there are reports on the use of excess amounts of VC for rGO sponge formation[38], the effect of higher GO:VC ratios on the processing and properties of rGO sponges has not been systematically studied. More importantly, as a reducing agent, the role of excess VC in controlling the structure of rGO sponges is relatively unknown. Higher GO concentration, acidic pH and temperatures of up to 95 °C, have been reported to favor the formation of robust sponges[38, 39]. The sponges of this study were formed at a GO concentration of 4 mg/mL, pH 3 and a temperature of 95 °C, to ensure that the resulting 3D structure possesses superior mechanical properties.

Adding excess amounts of VC significantly influenced the microstructure of the sponges. SEM micrographs of the freeze-fractured surfaces of rGO:VC sponges (Figure 1c–j) showed arrays of multi-scale and hierarchical pores. The sponges were comprised of large pores of hundreds of microns to one millimeter in diameter (milli-pores; Figure 1c, e, g and i), while the separating walls of these milli-pores consisted of submicron to few micrometer wide pores (micron-pores; Figure 1d, f, h and j). In other words, the milli-pores were located in a porous matrix comprised of micron-pores.

Increasing the VC content influenced the morphology of both milli- and micron-pores. By using excess amounts of VC, we observe that the large millipores evolve from barely distinguishable

(Figure 1c), to isolated (Figure 1e) and finally to an interconnected morphology (Figure 1g and i). The micron-pore morphology is equally influenced by the VC content. The wall micron-pores of the rGO:VC 50 sponge are randomly shaped and lack clear interconnectivity (Figure 1d), while in rGO:VC 100, these pores start to assemble into a honeycomb-like structure (Figure 1f). The morphology of micron-pores in rGO:VC 150 is very close to a honeycomb structure where a high density of well-packed and equi-sized pores is observed (Figure 1h). Further increasing the VC content in rGO:VC 200 resulted in high density of small interconnected circular pores which did not have the order and structure of rGO:VC 150 (Figure 1j).

The hierarchical nature of the pores in the rGO sponges is due to the use of excess VC. The solubility of VC in water is 330 g/L, whereas the concentration of VC in rGO:VC 50, rGO:VC 100, rGO:VC 150 and rGO:VC 200 sponges was 200, 400, 600 and 800 g/L, respectively. The excess VC could not be completely dissolved in the aqueous phase when the GO:VC ratio in the mixture exceeded approximately 1:80, especially considering the relatively high viscosity of concentrated GO dispersions. The morphological evolution of milli-pores also exhibited a correlation with the amount of undissolved VC grains; in rGO:VC 50 sponge, where the VC content is below its solubility, the milli-pores are barely distinguishable (Figure 1c), whereas increasing the VC content above the critical solubility ratio of 1:80, resulted in formation of some isolated milli-pores in rGO:VC 100 (Figure 1e), and well-defined and interconnected milli-pores in rGO:VC 150 (Figure 1g) and rGO:VC 200 (Figure 1i) sponges. The remaining granular VC acted as a soft template for the self-assembly of rGO sheets at the liquid/solid (water/VC) interface, resulting in full wrapping of VC grains with rGO sheets. The VC grains' soft templates were then dissolved during the post-synthesis washing of the sponges with copious amounts of deionized water, leaving large pores (milli-pores) behind (Figure 2a-c). The SEM micrograph of rGO:VC

150 sponge after the first post-synthesis water wash (Figure 2a) shows a milli-pore partially filled with VC. The outline of the milli-pore of interest has been highlighted with a black dashed line. The VC grain soft template occupying the milli-pore was partially dissolved and disintegrated after the first water wash. Examination of another milli-pore after the fifth water wash (Figure 2b) clearly shows major dissolution of the VC grain. The fact that the milli-pores are filled with solid material after freeze-drying and the shrinkage and dissolution of this solid material after successive water washes confirm the role of water soluble VC grains as soft templates. Based on these observations, the role of VC as a facile, cheap and multi-functional soft-template for formation of hierarchically porous rGO sponge is schematically summarized in Figure 2c.

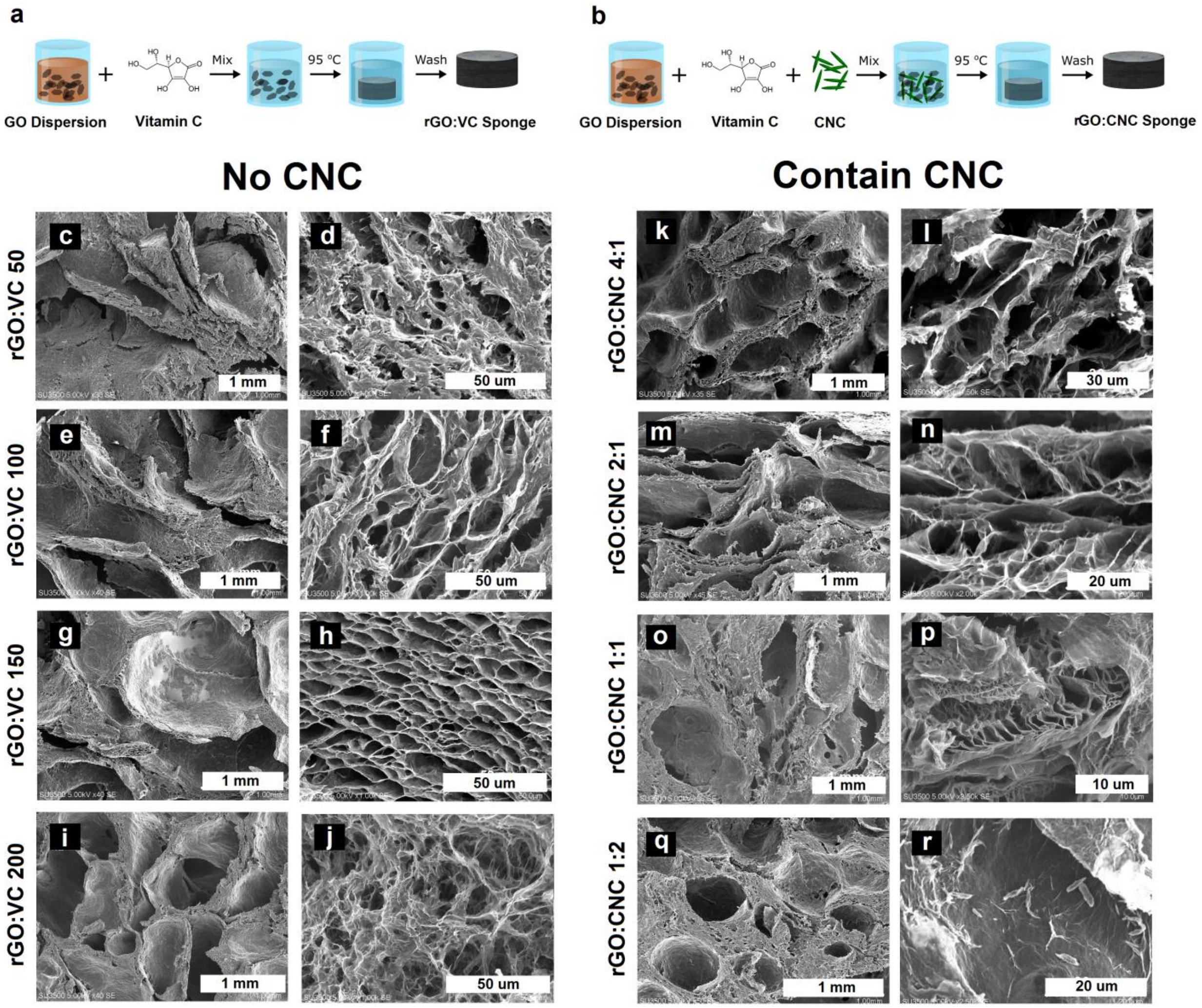

Figure 1. SEM micrographs of the freeze-fractured surfaces of rGO:VC and rGO:CNC sponges. Schematic representation of the processing method of (a) rGO:VC and (b) rGO:CNC sponges. The evolution of pore structure and morphology of (c–j) rGO:VC and (k–r) rGO:CNC sponges can be observed in the SEM micrographs of the freeze-fractured surfaces of these sponges.

3.2. CNCs inhibit the restacking of rGO sheets upon self-assembly into 3D sponges

Introducing CNCs to the sponges also significantly affected the morphology of the milli- and micron-pores. Because the pore morphology in rGO:VC 150 exhibited the desirable well-defined honeycomb structure, for formation of rGO:CNC hybrid sponges, the ratio of rGO:VC was fixed at 1:150 and different amounts of CNCs were used to evaluate their impact on pore structure. By increasing the CNC content, the walls separating the larger milli-pores became thicker and the pore sizes defined by them became smaller (Figure 1k, m, o and q). This is likely due to the accumulation of CNCs in the pore walls. The SEM images show that at higher CNC contents, the milli-pores start to become less interconnected (Figure 1o, q). Also, excessive amounts of CNCs (e.g., rGO:CNC 1:2) resulted in their aggregation (Figure 1r), which could possibly impact the mechanical properties of the sponges.

The transition of milli-pore size and their corresponding wall thickness can be clearly seen in sponges containing low (rGO:CNC 4:1, Figure 1k) and high amounts of CNCs (rGO:CNC 1:2, Figure 1q). At the micron-pore length scale, adding CNCs resulted in a larger and more exfoliated pore structure. CNCs expanded the space between pore walls (which is often comprised of multi-stacked rGO sheets) as a result of their anisotropic rod-shaped geometry and exfoliated them into accordion-shaped structures (Figure 1n and p). Strong hydrogen bonding between the partially reduced GO and CNCs is likely controlling their interaction.

The rGO:CNC 2:1 sponge was selected for more in-depth study because it presented a good balance of milli-pore interconnectivity, micron-pore exfoliation, and no signs of CNC aggregation. The rGO:CNC 2:1 sponge was cut in wet state by a razor blade to minimize the disruption of CNCs and was studied by SEM. The micrographs (Figure 2d) reveal that the CNCs self-assemble on rGO surfaces in the form of fibers of less than 5 µm in diameter (Figure 2d).

Since both rGO and CNCs are mostly carbonaceous materials, elemental analysis such as energy dispersive spectroscopy could not provide useful information on the nature of the self-assembled CNCs. To further examine this structure, the rGO:CNC 2:1 sponges were studied using TEM (Figure 2e). In a typical TEM micrograph (Figure 2e), a stacked and wrinkled rGO background can be seen (indicated as rGO in Fig. 2e), on top of which CNC nanorods have self-assembled into fibers of 1-5 µm diameter (indicated as CNC in Fig. 2e). Based on these observations, in the course of sponge formation, CNCs self-assemble into micron-sized fibers and attach to rGO nanosheets.

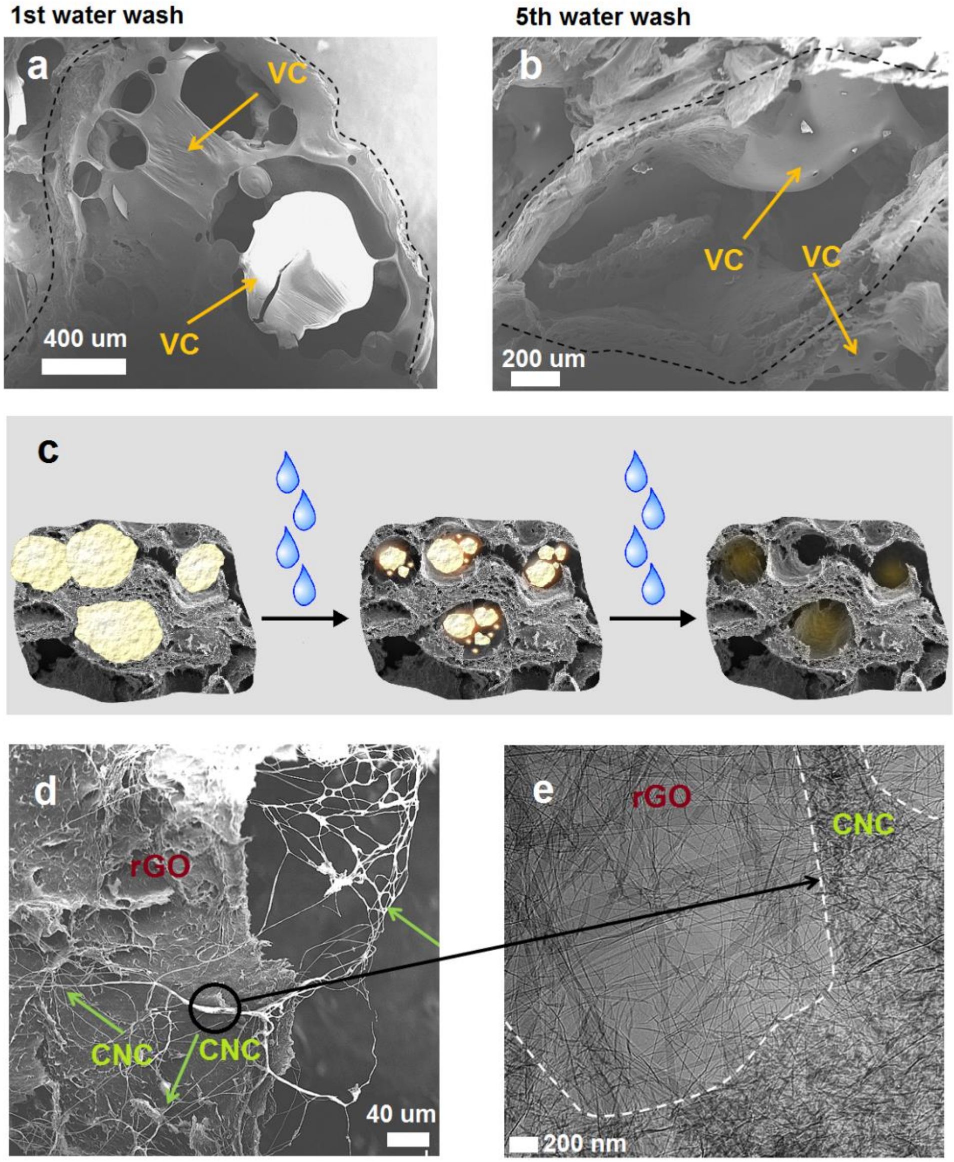

Figure 2. Formation mechanisms of rGO:VC and rGO:CNC sponges. SEM micrographs of a rGO:VC 150 sponge after (a) first, and (b) fifth water wash reveal the gradual and selective dissolution of VC grains (orange arrows) as (c) depicted schematically. The dashed black lines in (a) and (b) mark the outer boundary of typical milli-pores. The CNC nanorods in rGO:CNC 2:1 sponge self-assemble to form a 3D structure (green arrows) on rGO as evidenced by (d) SEM, and (e) TEM micrographs. The white dashed

line in (e) denotes the boundary of a typical fiber marked by a black circle in (d), which is formed by self-assembly of CNC nanorods.

The unique pore structure of the rGO:CNC 2:1 sponge and its non-CNC containing counterpart rGO:VC 150, was studied using X-ray tomography at different scales (microCT and nanoCT) (Figure 3). The difference in electron density between wall (comprised of rGO or rGO-CNC) and pores (comprised of air) provides sufficient absorption contrast for attenuation based X-ray imaging. Rendered 3D reconstructions from microCT are shown in Figure 3b and d alongside representative segmented 2D slices that illustrate the detailed pore network in these samples (Figure 3a, c). The 3D reconstructions allowed us to study the pore structure and their interconnectivity at any given point or angle of the sponges, thus enabling us to comment on the statistical distribution of the pores within the sponges– an analysis that would be extremely cumbersome and inaccurate to perform by solely relying on SEM images. Videos of the 3D reconstructed sponges, giving a 360° view of the samples, are provided as supplementary multimedia files.

In line with SEM observations, adding CNCs resulted in thicker and denser pore walls (Figure 3 a–d). Since the fine details of micron-pores were not readily evident in microCT reconstructions, the micron-pores in rGO:CNC 2:1 were scanned and reconstructed with a high resolution nanoCT device (Figure 3f). The interconnected nature of the micron-pores is clearly visible in the nanoCT reconstruction (refer to supplementary multimedia files for a 360° video of this sponge).

Since microCT provides a unique opportunity to visualize almost all of the pores in a relatively large volume of the sponge, the chord length distribution (CLD), a function which is proportional to the pore size distribution of the sponges, was calculated (Figure 3e). Both samples show a bimodal CLD, confirming the hierarchical pore structure observations from SEM imaging. Based on the CLD analysis, the modes of micron- and milli-pore sizes of the rGO:VC 150 sponge (no CNC) were found at 43 and 647 μm, respectively (total average pore size was 1038 μm). The modes of micron- and milli-pore sizes of the rGO:CNC 2:1 sponge were comparable with values of 40 and 650 μm (total average pore size was 1011 μm). However, the frequency associated to the mode of the micron-pores for the rGO:CNC 2:1 sponge was lower than that of the rGO:VC 150 sample.

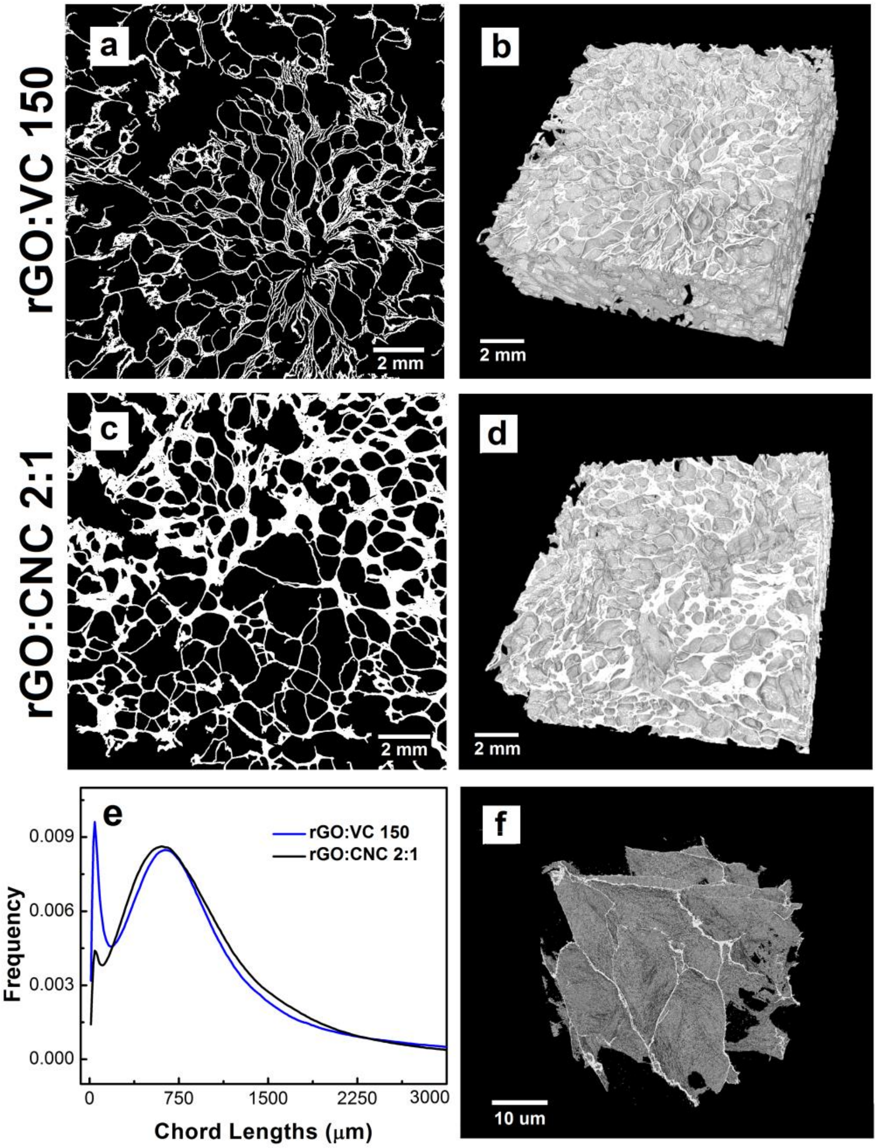

Figure 3. X-ray tomography images and bimodal chord length distribution. (a), (c) Segmented 2D slices from microCT, and (b), (d) 3D renderings of microCT images of rGO:VC 150 and rGO:CNC 2:1 sponges. In line with SEM observations, (e) the calculated chord length distributions reveal a bimodal (hierarchical) pore structure. (f) NanoCT 3D reconstructions of the sponges give a much higher resolution (voxel sidelength of 48.4 nm) compared to microCT (voxel sidelength of 10.79 μm) and thereby provide better insight into the architecture of the micron- and milli-sized pores.

3.3. Remarkable strengthening of hybrid sponges by 1D CNCs

Use of excess amounts of VC resulted in ultra-strong sponges with storage moduli ranging from 92 to 291 kPa at 10 Hz (Figure 4a). These values are 1-3 orders of magnitude larger than those reported in the literature for single-component GO and rGO sponges (see Table S1 for a summary of literature data and its comparison with our results). While increasing the VC content of the sponges resulted in well-defined and more ordered porous structures, it had an inverse effect on the storage modulus of the sponges. Figure 4a shows that the storage modulus of the sponges decreased with increasing VC content over a wide range of frequencies. The decrease in storage modulus could be a result of the large porosity (and lower apparent density) of high VC content sponges, whereas low VC content sponges such as rGO:VC 50 were less porous and denser. In high VC content sponges, the VC was washed out after sponge formation, leaving behind large pores which decreased the storage modulus of the sponges. However, adding CNCs to the sponges compensated for the loss of storage modulus at high VC content (Figure 4b). Introduction of CNCs successfully reinforced the sponges whereby the storage moduli of rGO:CNC 2:1 and rGO:CNC 4:1 were approximately 6 and 2.5 fold larger than their non-CNC containing counterpart rGO:VC 150, respectively (Figure 4). The self-assembly of CNCs on rGO, as shown in Figure 2d and e is the main reason behind the significant increase in the storage moduli of the CNC containing sponges. However, increasing the CNC content to larger values (e.g., in rGO:CNC 1:1 and rGO:CNC 1:2) resulted in the deterioration of the mechanical properties due to aggregation of CNCs and a decrease of order in the pore wall structure, as evident by SEM micrographs (Figure 1). The exceptionally high storage modulus of ~800 kPa at 10 Hz for rGO:CNC 2:1 is one of the highest values reported in the literature for rGO sponges (Table S1 in Supporting Information). Moreover, this ultra-strong sponge was synthesized using a mild formation process at low temperature and near ambient pressure. To study the effect of formation temperature, the rGO:CNC 2:1 sponges were also formed at 45 and 60 °C. The storage moduli of these sponges were lower than the rGO:CNC 2:1 sample formed at 95°C, confirming the key effect of formation temperature on the mechanical properties of the sponges (Figure S2). Since rGO:CNC 2:1 had a desirable combination of porous microstructure and strong mechanical properties, it was chosen for studying contaminant removal from water (section 3.5).

The mechanical properties of the rGO:CNC 2:1 sponge were also studied in the compression mode using DMA. The sponge demonstrated a (visco)elatic response before it reached its yield point of ~120 kPa at ~7.5% strain, after which it plastically deformed (Figure 4c). The cyclic load-unload response of the rGO:CNC 2:1 sponge was studied at a maximum stress below (60 kPa) and above (140 kPa) its yield strength to evaluate the compressibility and recoverability of the sponges under elastic and plastic deformations (Figure 4d). When subjected to loading below its yield strength (red curve in Figure 4d), the sponge showed very good compressibility and complete recovery of deformation after 3 load-unload cycles. Cyclic loading of the sponge above its yield strength (blue curve in Figure 4d) resulted in permanent deformation above the yield point in the first cycle; however, apart from the initial ~7.5% strain due to yielding, the sponge showed very good compressibility and recovery in the following load-unload cycles.

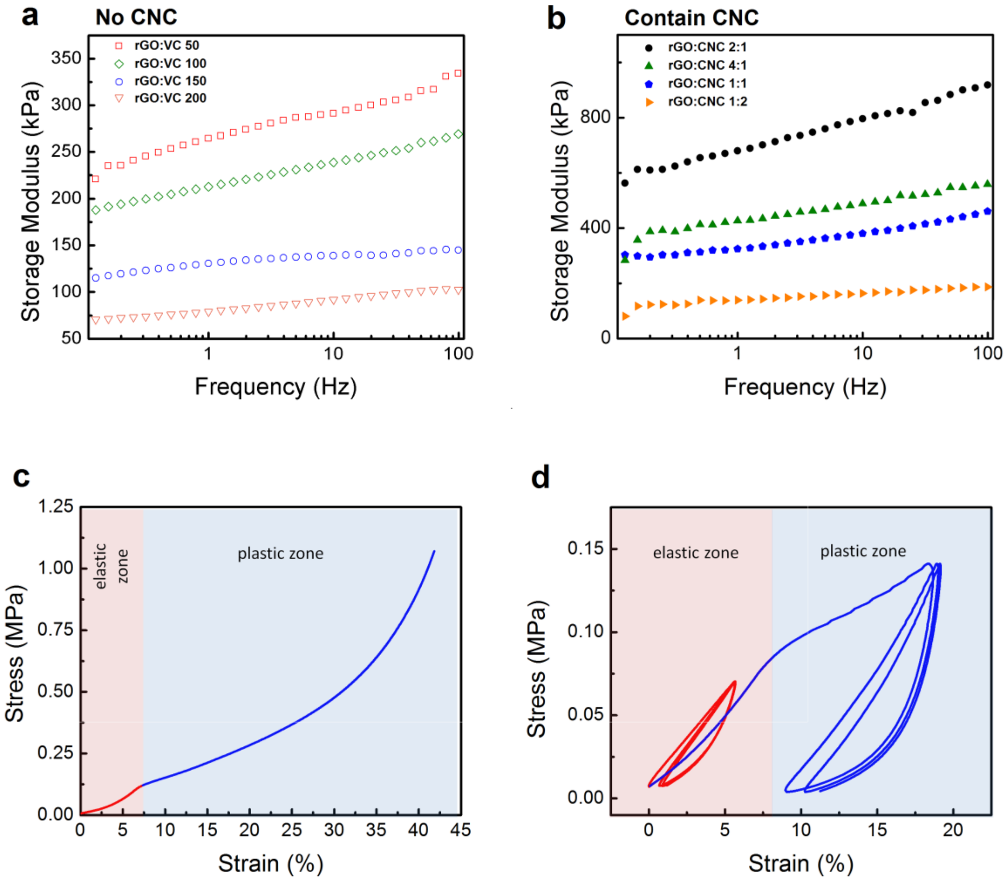

Figure 4. The storage moduli of sponges. Comparing the storage moduli of (a) rGO:VC and (b) rGO:CNC sponges revealed the strengthening role of CNCs in hybrid sponges. In (b), the ratio of rGO:VC is 1:150. (c) Typical static stress-strain curve of rGO:CNC 2:1 sponge reveals (visco)elastic and plastic deformation zones. (d) rGO:CNC 2:1 sponge demonstrates stable cyclic load-unload behavior under elastic and plastic regimes.

3.4. Surface chemistry of sponges

Prior to conducting experiments on contaminant removal from water, the surface chemistry of the formed sponges was examined by XPS and Raman spectroscopy. XPS C_{1s} peaks were deconvoluted to their constituent sub-peaks at 284.7 (sp^2 carbon, C=C), 285.5 (sp^3 carbon, C–C), 286.7 (hydroxyl, C–OH), 287.6 (carbonyl and epoxide, C=O/C–O–C) and 289 eV (carboxyl, O=C–OH) (Figure 5a-c and Table 1). GO nanosheets were initially rich in oxygen-containing functional groups. Reduction with VC resulted in a significant decrease of the number of carbonyl/epoxide groups and the restoration of sp^2 domains, which is in line with similar reports of VC reduction of GO[37, 38]. Reduction of functional groups was negligible in the rGO:VC 1 sponge as the amount of VC was below the stoichiometric ratio. When the VC content was further increased in the rGO:VC 10 sponge, the amount of carbonyl/epoxide and carboxyl groups decreased significantly.

Table 1. Deconvolution of C_{1s} peaks and Raman D/G ratio of sponges

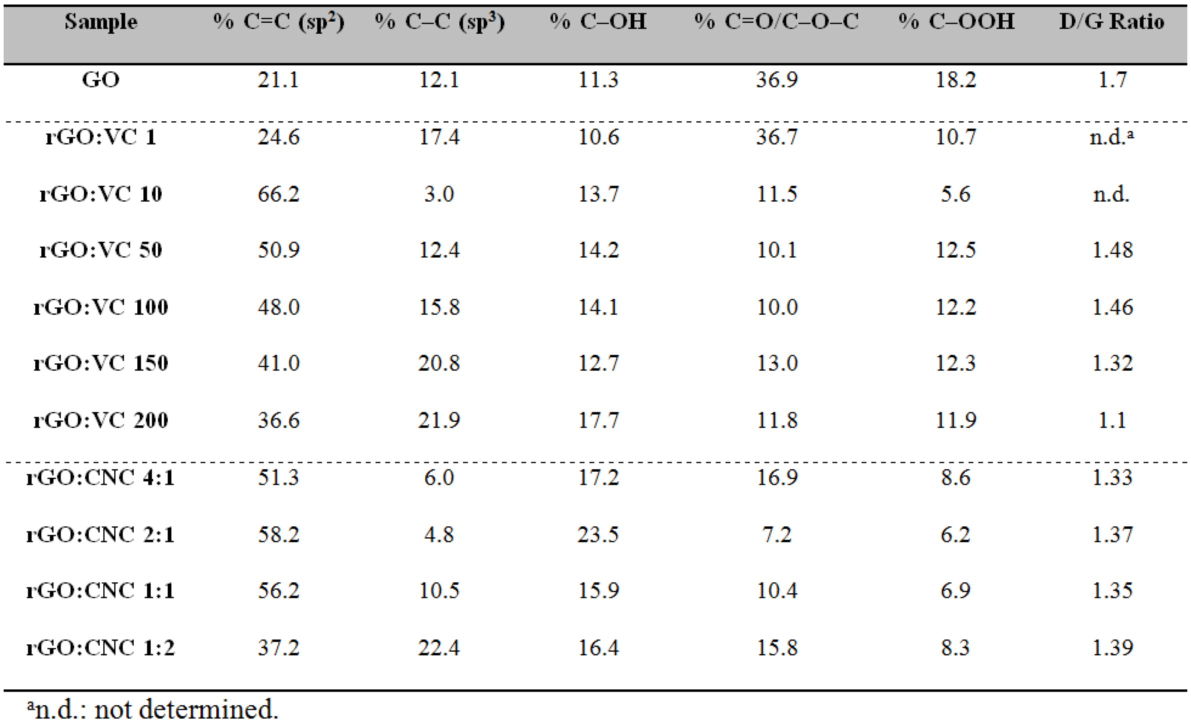

Sample	% C=C (sp^2)	% C–C (sp^3)	% C–OH	% C=O/C–O–C	% C–OOH	D/G Ratio
GO	21.1	12.1	11.3	36.9	18.2	1.7
rGO:VC 1	24.6	17.4	10.6	36.7	10.7	n.d.[a]
rGO:VC 10	66.2	3.0	13.7	11.5	5.6	n.d.
rGO:VC 50	50.9	12.4	14.2	10.1	12.5	1.48
rGO:VC 100	48.0	15.8	14.1	10.0	12.2	1.46
rGO:VC 150	41.0	20.8	12.7	13.0	12.3	1.32
rGO:VC 200	36.6	21.9	17.7	11.8	11.9	1.1
rGO:CNC 4:1	51.3	6.0	17.2	16.9	8.6	1.33
rGO:CNC 2:1	58.2	4.8	23.5	7.2	6.2	1.37
rGO:CNC 1:1	56.2	10.5	15.9	10.4	6.9	1.35
rGO:CNC 1:2	37.2	22.4	16.4	15.8	8.3	1.39

[a] n.d.: not determined.

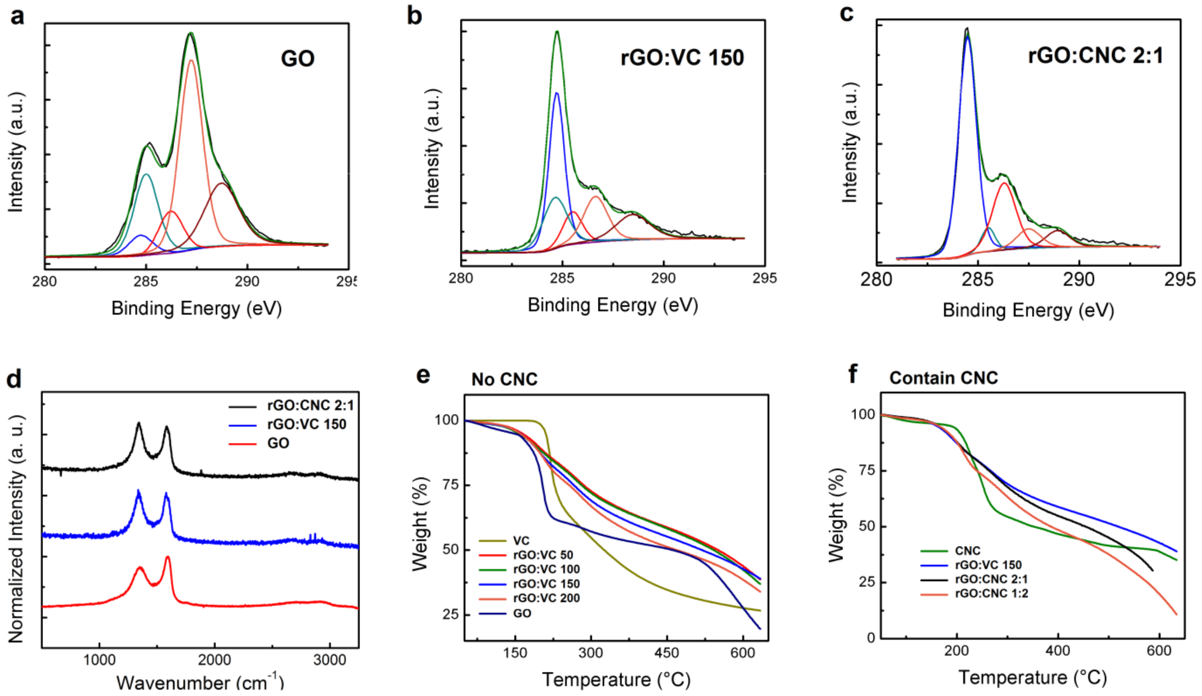

Figure 5. Surface chemistry and composition of the sponges. XPS C_{1s} peaks of (a) GO, (b) rGO:VC 150 and (c) rGO:CNC 2:1 sponges deconvoluted into sp^3 (—) and sp^2 (—) hybridized carbons, hydroxyl (—), carbonyl/epoxide (—) and carboxyl (—) sub-peaks, (d) Raman spectra of the same samples. The composition of (e) rGO:VC, and (f) rGO:CNC sponges was investigated by TGA.

A further increase in the amount of VC did not result in a higher degree of reduction; the change in the relative amount of sp^2 and sp^3 hybridized carbon is due to the existence of excess VC in the sponge structure, where the sp^3 hybridized carbons of free VC are contributing to the increase in the amount of sp^3 carbons.

Introduction of CNCs resulted in a slight increase in the amount of hydroxyl groups and reduction in the amount of carboxyl and epoxide groups in rGO:CNC 2:1 sponge versus rGO:VC 150 (Figure 5b and c, and Table 1). The CNCs used in this study were rich in hydroxyl groups (Figure S3 in

Supporting Information) and thus, resulted in the slight increase in the amount of hydroxyl groups within the hybrid sponges. Similarly, due to the sp^3 hybridized backbone of CNCs, increasing CNC content resulted in the relative amount of the sp^3 in the hybrid sponges to be skewed towards larger values. Furthermore, adding CNCs did not interfere with the reduction mechanism of VC on GO nanosheets; VC was shown to mostly reduce carbonyl/epoxide groups in both rGO:VC and rGO:CNC sponges (Table 1). The XPS analysis of rGO:CNC 2:1 sponges formed at 45 and 60 °C showed values close to the sample formed at 95 °C (Table S2); thus, processing temperature did not affect the surface chemistry of the sponges.

Raman spectroscopy of the sponges also revealed that the ratio of D (~1340 cm^{-1}) to G band (~1580 cm^{-1}) of the rGO:VC samples decreased by increasing the VC content, due to reduction of the samples by VC (Table 1 and Figure 5d). Adding CNCs did not affect the D/G ratio of the rGO:CNC sponges.

Chemical reduction of GO by VC and successful incorporation of CNCs into the hybrid sponges were also investigated by TGA (Figure 5e and f). Upon heating in nitrogen atmosphere, there is sharp weight loss in the 160–220 °C range due to decomposition of the oxygen-containing functional groups of GO. In line with XPS and Raman results, the weight loss in the mentioned temperature range is not as pronounced for rGO:VC sponges (Figure 5e), once again confirming the role of VC in partial chemical reduction of GO.

Since both CNCs and rGO have negatively charged carboxyl groups, the electrostatic repulsion between them could potentially lead to the leaching of CNCs from the sponge structure during the final washing step; however, TGA thermograms (Figure 5f) confirmed that significant amounts of CNCs are immobilized in the hybrid sponge structure. The spreading of weight loss profiles of

CNC-containing (rGO:CNC) sponges above the onset of decomposition of pure CNCs (~210 °C), their deviation from the negative control (rGO:VC 150) sponge and the larger weight loss of the rGO:CNC 1:2 sponge that contains more CNCs than the rGO:CNC 2:1 sponge confirm that CNCs were successfully embedded into the sponges. Given the carboxyl- and hydroxyl-rich surface of CNCs and the abundance of hydroxyl and carboxyl groups on rGO (see XPS results in Table 1), hydrogen bonding could be a major driving force for the attachment of CNCs onto rGO nanosheets in the hybrid sponges.

3.5. Application of ultra-strong hybrid sponges: Removal of pollutants from contaminated water

The adsorptive performance of the sponges was evaluated using a series of classical and emerging contaminants. MB, a cationic dye, is widely used as a model pollutant for assessing the adsorptive properties of carbon-based materials and structures[41, 42]. The rGO:CNC 2:1 sponge showed an adsorption capacity of ~850 mg MB/g rGO, which is among the highest values reported in the literature for sponges with GO or rGO as sole adsorption materials (Table S3). It will be shown that the adsorption of MB on rGO:CNC 2:1 sponge follows a Langmuir isotherm model (Figure S4b). One of the fundamental assumptions of the Langmuir model is that a monolayer surface coverage of the adsorbate is obtained. It has previously been shown that the active surface area of rGO sponges in wet state can be determined by adsorption of MB whereby the area occupied by a single MB molecule is ~130 $Å^2$ [43-47]. Thus, the equivalent monomolecular surface area occupied by MB on the rGO:CNC 2:1 sponge in wet state is calculated to be ~2080 m^2/g. The advantage of determining the surface area in wet state as opposed to dry state is that the necessary freeze-drying step to obtain dry sponges can potentially result in the restacking of the rGO sheets and lead to significant under-estimation of the surface area[47], whereas in applications where rGO sponges are entirely used in water, it is more desirable to measure their surface area, among other properties, in wet state. A comparison between the MB adsorption capacity of various GO and rGO based sponges reported in the literature and our rGO:CNC 2:1 sponge based on their specific surface area reveals that the rGO:CNC 2:1 sponge has the highest adsorption capacity (Figure 6b).

The kinetic parameters obtained from modelling the adsorption behavior of sponges (i.e., the rate constant, k and equilibrium adsorption capacity, $q_{e,calc}$) for different contaminants are summarized in Table 2. The adsorption of MB molecules onto rGO:CNC 2:1 sponges followed pseudo-second order kinetics which indicated a chemisorption mechanism of interaction between MB molecules and the sponge surface (Figure S4a in SI). The adsorption of MB on GO and rGO-based sponges and other carbon-based materials such as activated carbon, GO and rGO nanosheets has been reported to follow pseudo-second order kinetics[48-50]. The adsorption kinetics of the rGO-CNC sponge for MB are 48-fold faster (Figure S5) and the maximum adsorption capacity is at least 2-fold higher (Table S4) than granular activated carbon (GAC) which is an industry standard in water contaminant removal. The significantly faster kinetics and higher adsorption capacity, in addition to the extremely low apparent density of the hybrid sponge (~0.01 g/cm^3 for rGO:CNC 2:1 sponge versus 0.48 g/cm^3 for GAC) makes it an ideal candidate for industrial water and wastewater treatment.

The adsorption isotherms for MB uptake by rGO:CNC 2:1 were also measured and a regression analysis using Langmuir and Freundlich adsorption models revealed that the Langmuir model best describes the adsorption of MB on the rGO:CNC 2:1 surface (Figure S4b,c in SI). Thus, MB molecules form a monolayer on the active sites of the sponges and the maximum adsorption capacity is controlled by the availability of free adsorption sites on the surface.

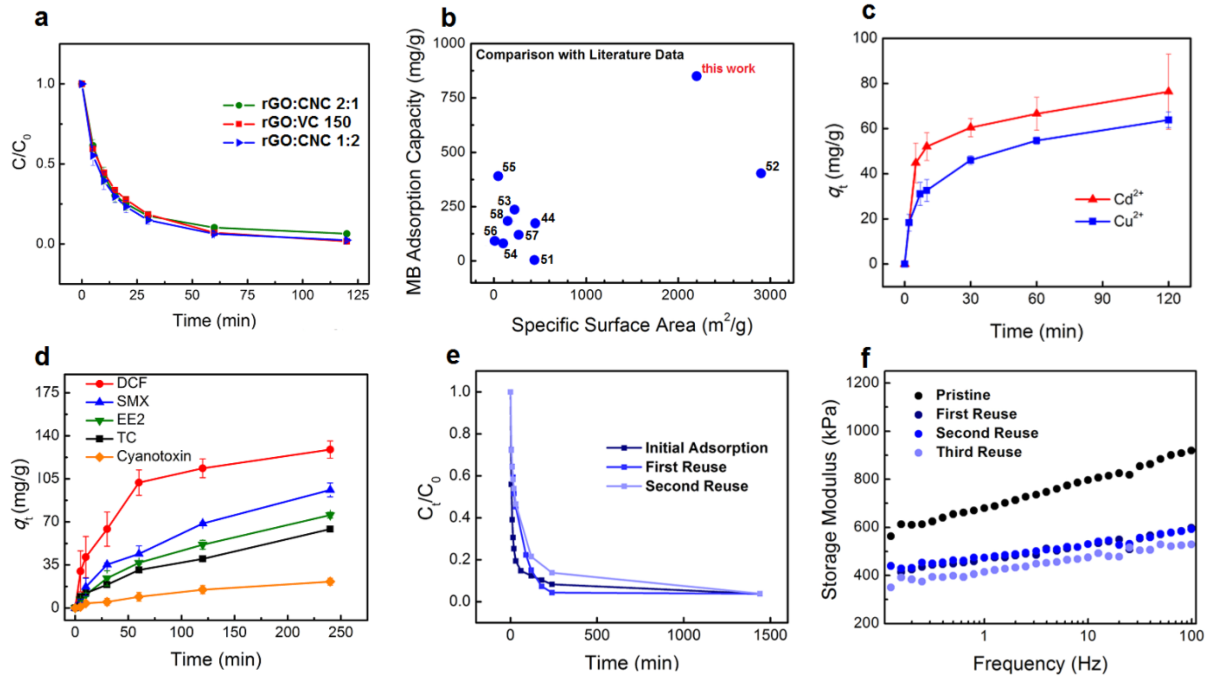

Figure 6. The contaminant adsorption performance and reusability of sponges. (a) The adsorption kinetics of MB by different rGO sponges; (b) comparison of MB adsorption capacity between rGO:CNC 2:1 sponge and other rGO-based sponges in literature[44, 51-58]; the adsorption kinetics of (c) Cu^{2+} and Cd^{2+} heavy metals ions, and (d) emerging pharmaceutical contaminants such as diclofenac (DCF), sulfamethoxazole (SMX), 17-α-ethynylestradiol (EE2), tetracycline (TC) and microcystin-LR (cyanotoxin) by rGO:CNC 2:1 sponges from aqueous solutions. The performance of sponges in terms of (e) MB adsorption kinetics, and (f) storage modulus was evaluated after multiple reuse cycles.

Levels of dissolved heavy metals in water supplies are of increasing concern due to their widespread occurrence and documented toxicity[59, 60]. Batch adsorption experiments were performed to evaluate the removal of Cu^{2+} and Cd^{2+} by the rGO-CNC 2:1 sponge. In the case of

Cu^{2+}, for an initial concentration of 50 mg/L, the system approaches equilibrium in approximately 2 h (Figure 6c), with a maximum adsorption capacity of 63.8 mg/g rGO (~1 mmol/g rGO). For the same initial Cd^{2+} concentration, the system reaches equilibrium at approximately the same time and a maximum adsorption capacity of 76 mg/g rGO (~0.8 mmol/g rGO). Normalizing the adsorption capacity of the sponges by the molar weights of the heavy metals reveals that the sponges had a higher affinity for Cu^{2+} than Cd^{2+}. GO and rGO have been shown to have a higher affinity towards Cu^{2+} over Cd^{2+} due to the larger electronegativity of copper ions and higher stability constant of its hydroxides and acetates (the complexes it forms with hydroxyl and carboxyl groups of rGO and CNCs) in comparison to its cadmium-based counterpart[61]. The adsorption kinetics of Cu^{2+} and Cd^{2+} are best fit by the pseudo-second order kinetic model (Table 2), which corresponds with previous kinetics studies for adsorption of copper ions onto carbon-based material[62, 63]. The presence of ion chelating groups such as hydroxyls and carboxyls on both rGO and CNCs is the reason behind the sponge's affinity to the metal ions. The adsorption capacity of the rGO-CNC sponge for these heavy metals from water is at least 3-fold higher than GAC (Table S4).

Discharge of pharmaceutical compounds and other emerging contaminants into water resources has created significant challenges for wastewater treatment plants as most are not equipped with tools to remove this new class of pollutants[64, 65]. The rGO:CNC 2:1 sponge successfully adsorbed a variety of common pharmaceuticals such as antibiotics (SMX and TC), an anti-inflammatory drug (DCF) and a hormone (EE2) (Figure 6d) as a result of its versatile chemistry. The adsorption of microcystin-LR (cyanotoxin), a toxin produced by cyanobacteria is also investigated. The sp^2 hybridized carbons of rGO, the basal plane hydroxyl groups and the negatively charged edge carboxyl groups of rGO and CNCs participate in contaminant adsorption through a variety of mechanisms including π–π stacking, hydrogen bonding and electrostatic interactions, respectively.

Table 2. Comparison of the pseudo-first and pseudo-second order kinetics adsorption rate constants and calculated and experimental q_e values

Contaminant	$q_{e,exp}$ (mg·g^{-1})	**Pseudo-first order**			**Pseudo-second order**		
		$q_{e,cal}$ (mg·g^{-1})	k_1 (min^{-1}×10^{-2})	R^2	$q_{e,cal}$ (mg·g^{-1})	k_2 (g·mg^{-1}·min^{-1}×10^{-4})	R^2
MB	178.2	75.6	2.00	0.927	181.9	9.80	0.999
Cu^{2+}	63.8	47.4	2.93	0.937	65.8	39.10	0.989
Cd^{2+}	76.3	65.5	4.52	0.844	84.4	4.95	0.994
DCF	128.8	106.9	1.52	0.988	126.6	4.83	0.975
SMX	96.0	89.5	0.93	0.976	106.4	2.53	0.962
TC	148.8	138.7	3.75	0.996	134.9	7.69	0.905
EE2	117.2	94.1	0.58	0.995	112.4	1.40	0.902
Cyanotoxin	21.4	23.0	1.20	0.988	27.9	8.66	0.913

The adsorption kinetics of emerging contaminants (SMX, TC, DCF and EE2) best fit a pseudo-first order model (physisorption). The cyanotoxin follows a pseudo-first order model, suggesting a physical adsorption process; likely a hydrogen bonding. The adsorption capacity of the rGO:CNC 2:1 sponge for the different pharmaceuticals is also considerably higher than GAC (with the exception of TC) (Table S4).

Mechanical robustness is one the major obstacles to practical implementation of GO and rGO sponges for domestic and urban water treatment. Given the superior mechanical properties, low density, and remarkable multifunctional performance of rGO:CNC 2:1 sponge in contaminant removal from water, its reusability was investigated by multiple cycles of adsorption and desorption of MB (Figure 6e). At the end of each adsorption-desorption cycle, the equilibrium adsorption capacity remained unaffected, leading to an eventual complete uptake of MB from solution. The adsorption rate after each cycle was slightly decreased; however, this reduction was by no means prohibitive in effective removal of MB. The storage moduli of the sponges were also measured at the end of each cycle. While the first regeneration of the sponge resulted in ~20% decrease in the modulus of the sponge (at 10 Hz), further regeneration cycles only slightly affected the moduli of the sponges (Figure 6f).

4. Conclusions

Ultra-strong and highly adsorptive hybrid rGO-CNC sponges were processed using a facile green synthesis method with VC at low temperature and near ambient pressure. VC not only acted as a green reducing and gelling agent, but also directed the assembly of the rGO nanosheets into hierarchically porous 3D sponges. The use of excess VC resulted in the selective wrapping of the undissolved VC grains with rGO sheets, creating milli-pores when the VC was dissolved with water. At a much smaller length scale, the self-assembly of rGO as a result of VC reduction at 95 °C resulted in well-ordered pores of several micrometers in diameter (micron-pores). CNCs contributed to the mechanical integrity of the sponges by providing a robust scaffold that held the rGO nanosheets in place. The interplay between the roles of VC and CNC contents in the sponges provided an effective tool to tailor the microstructure and the properties of the sponges. By optimizing the amount of VC and CNC, an ultra-strong sponge with an exceptional storage modulus of 800 kPa and a remarkable MB adsorption capacity of 850 mg/g rGO was processed.

The reusable sponge also showed excellent adsorption capacity towards heavy metal ions, pharmaceuticals and emerging contaminants.

Conflicts of interest

Authors N. Tufenkji, N. Yousefi, Z. Hosseinidoust and K. K. W. Wong have applied for a patent (PCT/CA2017/050983) on the preparation of nanocomposite hydrogels and their use in purification of a fluid.

Acknowledgements

We are grateful to Prof. S.L.S. Stipp for suggesting the use of X-ray tomography for characterization of the sponge materials, P. Hubert and L. Riffard for use of the rheometer, M. Kamal for use of the TGA, M. Cerruti for use of the Raman microscope, A. Angulo, K. Lawless and M. A. E. de Franco for assistance in sponge synthesis and contaminant adsorption tests, N. Lin for preparation of graphics, and J. Beil and K. N. Dalby for support collecting nanoCT data. We thank the Japan Synchrotron Radiation Research Institute for the allotment of beam time on beamline BL37XU of SPring-8 (Proposal 2016B1626) and Dr. Y. Terada and Dr. K. Uesugi for technical support. Funding for travel to the synchrotron facility was provided by the Danish Agency for Science, Technology and Innovation via Danscatt. H.O.S and S.B. acknowledge financial support from the P^3 project funded by Innovation Fund Denmark and Maersk Oil and Gas. N.Y. acknowledges financial support from a McGill Engineering Doctoral Award and N.T. acknowledges support from the Canada Research Chairs Program and the Natural Sciences and Engineering Research Council of Canada.

Supporting Information

The following Supporting Information is available online:

- 3D reconstruction of millimeter-sized pore structure of rGO:CNC 2:1 sponges using microCT (video)
- 3D reconstruction of micron-sized pore structure of rGO:CNC 2:1 sponges using nanoCT (video)
- Supplementary figures and tables (PDF)

References

1. R. Wang, C. Xu and J.-M. Lee, *Nano Energy*, 2016, **19**, 210-221.
2. C. Xiong, W. Zhong, Y. Zou, J. Luo and W. Yang, *Electrochim. Acta*, 2016, **211**, 941-949.
3. Z.-Y. Sui, C. Wang, Q.-S. Yang, K. Shu, Y.-W. Liu, B.-H. Han and G. G. Wallace, *J. Mater. Chem. A*, 2015, **3**, 18229-18237.
4. M. Zhang, Y. Wang and M. Jia, *Electrochim. Acta*, 2014, **129**, 425-432.
5. Y.-H. Zhao, Y.-F. Zhang, S.-L. Bai and X.-W. Yuan, *Composites, Part B*, 2016, **94**, 102-108.
6. V. Chabot, D. Higgins, A. Yu, X. Xiao, Z. Chen and J. Zhang, *Energy Environ. Sci.*, 2014, **7**, 1564-1596.
7. H. Li, J. Fan, Z. Shi, M. Lian, M. Tian and J. Yin, *Polymer*, 2015, **60**, 96-106.
8. Y. Shen, Q. Fang and B. Chen, *Environ. Sci. Technol.*, 2014, **49**, 67-84.
9. J. S. Bunch, S. S. Verbridge, J. S. Alden, A. M. Van Der Zande, J. M. Parpia, H. G. Craighead and P. L. McEuen, *Nano Lett.*, 2008, **8**, 2458-2462.
10. J. H. Lee, D. W. Shin, V. G. Makotchenko, A. S. Nazarov, V. E. Fedorov, Y. H. Kim, J. Y. Choi, J. M. Kim and J. B. Yoo, *Adv. Mater.*, 2009, **21**, 4383-4387.
11. X. Yang, L. Qiu, C. Cheng, Y. Wu, Z. F. Ma and D. Li, *Angew. Chem., Int. Ed.*, 2011, **50**, 7325-7328.
12. Z. D. Huang, B. Zhang, R. Liang, Q. B. Zheng, S. W. Oh, X. Y. Lin, N. Yousefi and J. K. Kim, *Carbon*, 2012, **50**, 4239-4251.
13. Z. D. Huang, B. Zhang, S. W. Oh, Q. B. Zheng, X. Y. Lin, N. Yousefi and J. K. Kim, *J. Mater. Chem.*, 2012, **22**, 3591-3599.
14. M. Hussain, M. Kabir and A. Sood, *Curr. Sci.*, 2009, **96**, 664-673.
15. P. Wick, P. Manser, L. K. Limbach, U. Dettlaff-Weglikowska, F. Krumeich, S. Roth, W. J. Stark and A. Bruinink, *Toxicol. Lett.*, 2007, **168**, 121-131.
16. Z. Hosseinidoust, M. N. Alam, G. Sim, N. Tufenkji and T. G. M. Van De Ven, *Nanoscale*, 2015, **7**, 16647-16657.
17. A. W. Carpenter, C. F. De Lannoy and M. R. Wiesner, *Environ. Sci. Technol.*, 2015, **49**, 5277-5287.
18. M. Mariano, N. El Kissi and A. Dufresne, *J. Polym. Sci., Part B: Polym. Phys.*, 2014, **52**, 791-806.

19. H. Bi, X. Xie, K. Yin, Y. Zhou, S. Wan, L. He, F. Xu, F. Banhart, L. Sun and R. S. Ruoff, *Adv. Funct. Mater.*, 2012, **22**, 4421-4425.
20. Y. Wu, N. Yi, L. Huang, T. Zhang, S. Fang, H. Chang, N. Li, J. Oh, J. A. Lee and M. Kozlov, *Nat. Commun.*, 2015, **6**, 6141.
21. Q. Zheng, Z. Cai and S. Gong, *J. Mater. Chem. A*, 2014, **2**, 3110-3118.
22. N. Yousefi, X. Lin, Q. Zheng, X. Shen, J. R. Pothnis, J. Jia, E. Zussman and J. K. Kim, *Carbon*, 2013, **59**, 406-417.
23. H. Yang, M. N. Alam and T. G. van de Ven, *Cellulose*, 2013, **20**, 1865-1875.
24. S. Bruns, T. Müllner, M. Kollmann, J. Schachtner, A. Höltzel and U. Tallarek, *Anal. Chem.*, 2010, **82**, 6569-6575.
25. S. Bruns, S. L. S. Stipp and H. O. Sørensen, *Adv. Water Resour.*, 2017, **105**, 96-107.
26. E. B. Knudsen, H. O. Sørensen, J. P. Wright, G. Goret and J. Kieffer, *J. Appl. Crystallogr.*, 2013, **46**, 537-539.
27. Y. Suzuki, A. Takeuchi, Y. Terada, K. Uesugi, R. Mizutani, M. D. de Jonge, D. J. Paterson and C. G. Ryan, 2016.
28. R. Chityala, K. R. Hoffmann, S. Rudin and D. R. Bednarek, 2005.
29. B. Münch, P. Trtik, F. Marone and M. Stampanoni, *Opt. Express*, 2009, **17**, 8567-8591.
30. D. Gürsoy, F. De Carlo, X. Xiao and C. Jacobsen, *J. Synchrotron Radiat.*, 2014, **21**, 1188-1193.
31. J. Courtois, M. Szumski, F. Georgsson and K. Irgum, *Anal. Chem.*, 2007, **79**, 335-344.
32. D. Cox, D. Hinkley, D. Rubin and B. Silverman, *Monographs on statistics and applied probability*, Springer, 1984.
33. T. Gosset, J.-L. Trancart and D. R. Thévenot, *Water Res.*, 1986, **20**, 21-26.
34. S. Lagergren, 1898.
35. F.-C. Wu, R.-L. Tseng, S.-C. Huang and R.-S. Juang, *Chem. Eng. J.*, 2009, **151**, 1-9.
36. G. Limousin, J.-P. Gaudet, L. Charlet, S. Szenknect, V. Barthes and M. Krimissa, *Appl. Geochem.*, 2007, **22**, 249-275.
37. M. Fernandez-Merino, L. Guardia, J. Paredes, S. Villar-Rodil, P. Solis-Fernandez, A. Martinez-Alonso and J. Tascon, *J. Phys. Chem. C*, 2010, **114**, 6426-6432.
38. J. Zhang, H. Yang, G. Shen, P. Cheng, J. Zhang and S. Guo, *Chem. Commun.*, 2010, **46**, 1112-1114.
39. W. Chen and L. Yan, *Nanoscale*, 2011, **3**, 3132-3137.
40. Z. Sui, X. Zhang, Y. Lei and Y. Luo, *Carbon*, 2011, **49**, 4314-4321.
41. M. Doğan, M. Alkan, A. Türkyilmaz and Y. Özdemir, *J. Hazard. Mater.*, 2004, **109**, 141-148.
42. N. Kannan and M. M. Sundaram, *Dyes Pigm.*, 2001, **51**, 25-40.
43. G. Kahr and F. Madsen, *Appl. Clay Sci.*, 1995, **9**, 327-336.
44. Y. Liu, T. Gao, H. Xiao, W. Guo, B. Sun, M. Pei and G. Zhou, *Electrochim. Acta*, 2017, **229**, 239-252.
45. D. N. Tran, S. Kabiri, T. R. Sim and D. Losic, *Environmental Science: Water Research & Technology*, 2015, **1**, 298-305.
46. W. Wan, R. Zhang, W. Li, H. Liu, Y. Lin, L. Li and Y. Zhou, *Environmental Science: Nano*, 2016, **3**, 107-113.
47. Y. Xu, Z. Lin, X. Huang, Y. Wang, Y. Huang and X. Duan, *Adv. Mater.*, 2013, **25**, 5779-5784.
48. S. S. Ashour, *J. Saudi Chem. Soc.*, 2010, **14**, 47-53.
49. P. Sharma, N. Hussain, D. J. Borah and M. R. Das, *J. Chem. Eng. Data*, 2013, **58**, 3477-3488.
50. S. Zamani and N. S. Tabrizi, *Res. Chem. Intermed.*, 2015, **41**, 7945-7963.
51. F. Canencia, M. Darder, P. Aranda, F. M. Fernandes, R. F. Gouveia and E. Ruiz-Hitzky, *Journal of Materials Science*, 1-13.
52. F. Liu, S. Chung, G. Oh and T. S. Seo, *ACS Appl. Mater. Interf.*, 2012, **4**, 922-927.
53. V. H. Luan, J. S. Chung, E. J. Kim and S. H. Hur, *Chem. Eng. J.*, 2014, **246**, 64-70.
54. J. Ma, C. Chen and F. Yu, *New Journal of Chemistry*, 2016, **40**, 3208-3215.

55. H. Sun, Z. Xu and C. Gao, *Adv. Mater.*, 2013, **25**, 2554-2560.
56. D. Wu, M. Yi, H. Duan, J. Xu and Q. Wang, *Carbon*, 2016, **108**, 394-403.
57. Z. Zhang, F. Xiao, Y. Guo, S. Wang and Y. Liu, *ACS Appl. Mater. Interfaces*, 2013, **5**, 2227-2233.
58. J. Zhao, W. Ren and H.-M. Cheng, *J. Mater. Chem.*, 2012, **22**, 20197-20202.
59. L. Järup, *Br. Med. Bull.*, 2003, **68**, 167-182.
60. D. Kar, P. Sur, S. Mandai, T. Saha and R. Kole, *Int. J. Environ. Sci. Technol.*, 2008, **5**, 119-124.
61. R. Sitko, E. Turek, B. Zawisza, E. Malicka, E. Talik, J. Heimann, A. Gagor, B. Feist and R. Wrzalik, *Dalton Trans.*, 2013, **42**, 5682-5689.
62. E. Demirbas, N. Dizge, M. Sulak and M. Kobya, *Chem. Eng. J.*, 2009, **148**, 480-487.
63. M. M. Rao, A. Ramesh, G. P. C. Rao and K. Seshaiah, *J. Hazard. Mater.*, 2006, **129**, 123-129.
64. N. Bolong, A. Ismail, M. R. Salim and T. Matsuura, *Desalination*, 2009, **239**, 229-246.
65. M. Petrović, S. Gonzalez and D. Barceló, *TrAC, Trends Anal. Chem.*, 2003, **22**, 685-696.

Graphical Abstract